

**Suction Effects of Craters Underwater**

Journal:	<i>Soft Matter</i>
Manuscript ID	SM-ART-08-2018-001601.R1
Article Type:	Paper
Date Submitted by the Author:	22-Sep-2018
Complete List of Authors:	Qiao, Shutao; The University of Texas at Austin, Department of Aerospace Engineering and Engineering Mechanics Wang, Liu; The University of Texas at Austin, Department of Aerospace Engineering and Engineering Mechanics Ha, KyoungHo; the University of Texas at Austin, Department of mechanical engineering Lu, Nanshu; University of Texas at Austin, Aerospace Engineering and Engineering Mechanics



1
2
3
4
5
6
7
8
9
10
11
12
13
14
15
16
17
18
19
20
21
22
23
24
25

Suction Effects of Craters Underwater

Shutao Qiao^{a,1}, Liu Wang^{a,1}, Kyoung-Ho Ha^b, Nanshu Lu^{*a, b, c, d}

^a*Center for Mechanics of Solids, Structures and Materials, Department of Aerospace Engineering and Engineering Mechanics, the University of Texas at Austin, Austin TX 78712, US.*

^b*Department of Mechanical Engineering, the University of Texas at Austin, Austin TX 78712, US.*

^c*Department of Biomedical Engineering, the University of Texas at Austin, Austin TX 78712, US.*

^d*Texas Materials Institute, the University of Texas at Austin, Austin TX 78712, US.*

1. S. Q. and L. W. contributed equally to this work.

* Corresponding author: nanshulu@utexas.edu, 512-471-4208, 210 E. 24th St, Austin, TX 78712

1
2
3
4
5
6
7
8
9
10
11
12
13
14
15
16
17
18
19
20

Abstract

Octopus-inspired cratered surfaces recently emerge as a new class of reusable physical adhesives. Preload-dependent adhesion and enhanced adhesion underwater distinct them from the well-studied gecko-inspired pillared surfaces. Despite growing experimental evidence, modeling framework and mechanistic understandings for cratered surfaces are still very limited. We recently developed a framework to evaluate suction forces produced by isolated craters in air. In this paper, we focus on underwater craters. The suction force-preload relation predicted by this framework has been validated by experiments carried out with incompressible fluid under small and moderate preload. Our model breaks down under large preload due to multiple possible reasons including liquid vaporization. Direct comparison between liquid and air-filled craters has been carried out and the dependence on the depth of water has been revealed. We find that the suction forces generated by underwater craters scale with specimen modulus but exhibit non-monotonic dependence on the aspect ratio of the craters.

Keywords: crater, underwater, adhesion, suction, negative pressure

1. Introduction

Adhesives that can stick and unstick repeatedly are called reversible or reusable adhesives. Reversible adhesives can find many applications such as wall mounts, foot pads for robots^{1, 2}, wafer handlers³⁻⁶, and bio-integrated electronics^{7, 8}. Desirable properties of reversible adhesives include fast and clean removal, tunable adhesion, as well as reliable attachment under both dry and wet conditions. Although permanent wet or underwater adhesives have undergone fast development^{9, 10}, strong but reversible underwater physical adhesives still remain challenging¹¹.

Full of microfibrils, gecko toe pads are found to be remarkable physical adhesives. Their adhesion strength was measured to be 100 kPa^{12, 13}, comparable to that of 3M scotch tapes (200 kPa). It has been revealed that the adhesion of microfibrils come from van der Waals interactions^{14, 15}. Contact mechanics has been applied to explain the enhanced adhesion when the fibril diameters decrease¹⁶. Extensive efforts have been made to produce gecko-mimetic artificial microfibrils¹⁷⁻¹⁹ and microspatula²⁰ as reusable adhesives. However, their adhesion strength is fixed once fabricated unless extra engineering is incorporated²¹⁻²³. It's also reported that wet surfaces or underwater environment impair the performance of microfibrils-enabled adhesives²⁴⁻²⁶. Therefore, alternative mechanisms are required for reversible adhesives with tunable adhesion in air and underwater.

The inspiration for reversible underwater adhesion comes from aquatic cephalopods such as squids and octopuses whose arms are equipped with hundreds of suckers²⁷⁻³⁰. For example, octopuses can easily anchor onto different terrains and substrates by actively manipulating muscles on their tentacles. Such attachment is enabled by the suction force due to the pressure difference between the sucker and the ambient, termed negative pressure, which can roar up to 300 kPa for octopuses and 800 kPa for decapods underwater^{31, 32}. The fact that microfibrils are found on the toe pads of lizards and insects while suckers evolved for marine animals implies that suction is more effective than van der Waals interactions underwater.

In fact, it is also our everyday experience that macroscopic suction cups are effective in attachment. Several papers already modeled thin-walled suction cups³³⁻³⁵. But macroscopic single suction cups are not flexible enough to conform to complex three-dimensional surfaces. While microscale suction cups have been built at the tip of micro-pillars³⁶⁻³⁹, the effect of van der Waals force versus suction force is still under debate^{38, 40, 41}. Moreover, slender micro-pillars suffer from notorious issues such as mechanical integrity after repetitive use⁴²⁻⁴⁵. As a result, in recent years, arrays of micro-craters emerged as a novel surface texture for reversible adhesion due to ease of fabrication, high conformability to curvilinear surfaces, and reusability. For example, in 2014, closely packed sub-micron-sized surface dimples on UV resin were reported with shear adhesive strength of 750 kPa under a preload of 3 N⁴, which is very competitive among

1 gecko-inspired dry adhesives⁴⁶. In 2015, Choi *et al.* fabricated 1- μm -diameter craters on the surface of
2 polydimethylsiloxane (PDMS) and measured the shear adhesive strength to be 1.6 kPa, higher than that of
3 the same PDMS with both flat surface or pillars on the surface⁷. In 2016, surface craters covered by a layer
4 of thermoresponsive hydrogel demonstrated switchable adhesion by heat, and was applied for transfer
5 printing of semiconducting nanomembranes⁵. In 2017, arrays of octopus-inspired micro-craters with built-
6 in protuberance structure demonstrated load-dependent adhesion under both dry and wet conditions⁴⁷,
7 distinct from that of gecko-like adhesives. Most recently, Baik *et al.* reported that micro-pillars with
8 concave tip geometry exhibit high dry/wet adhesion against both a smooth surface and rough, hairy skin³⁹.
9 Even when applied on irregular surfaces, nanosucker arrays flexible polydimethylsiloxane (PDMS) have
10 generated strong adhesion⁶.

11 Despite that many papers have attributed the strong attachment of cratered surfaces to suction effects⁵,
12 ⁴⁷⁻⁴⁹, there lacks comprehensive mechanistic understandings for the suction generation process, not to
13 mention the governing parameters. To date, only Baik *et al.*⁴⁷ has presented a closed-form solution for the
14 adhesion strength of cratered surfaces. However, this analysis is flawed as it is based on the prior work of
15 Afferrante *et al.*³³ and Tramacere *et al.*⁵⁰, which is only applicable to thin-walled suction cups rather than
16 craters. It is worth pointing out that craters are rather different from adhesives with microfluidic channels⁵¹
17 as craters are dimples on the surface which are surrounded by thick walls formed by the polymer matrix. In
18 our recent study⁵², we established the first theoretical framework to analyze isolated craters in air, obtained
19 nonlinear solutions to preload-dependent suction forces, and validated our solutions by experiments. We
20 have also unveiled the elasto-capillary effects on suction forces for miniature craters on soft polymers⁵³. At
21 this stage, to the best knowledge of the authors, no correct mechanistic understanding of underwater craters
22 has been established. Such an understanding is critical to the design and the prediction of cratered surfaces
23 working under wet condition. Building upon our established framework and experimental skills for dry
24 craters, herein we present a systematic study on the adhesion mechanism of an isolated crater underwater.
25 Our approach involves experimental, numerical, and analytical characterizations of isolated macroscopic
26 craters for which size effects associated with surface phenomena are negligible. We focus on spherical-cap-
27 shaped (SCS) craters, establish the suction-geometry, suction-preload, and suction-depth-of-water
28 dependence, and identify the limitation of our analysis by comparing with experimental results. When we
29 compare the suction effects of craters in both dry and wet conditions, we discover that the suction forces
30 generated by underwater craters can be significantly larger than dry craters of the same shape and material,
31 which explains the fact that most creatures utilizing suction for attachment are sea-lives.

32 This paper is organized as follows. In Section 2, we investigate the suction force produced by isolated
33 hemi-spherical craters. We study such craters based on experimental, numerical simulation, and analytical

1 approaches. After confirming the validity of our model, we then adopt the modeling framework for
 2 characterizing more general SCS craters. In Section 3, we calculate the suction forces of SCS craters of
 3 different shapes and at different preloads and compare them with experimental measurements, through
 4 which we identify the applicability of our model. In Section 4, we provide a brief summary of our key
 5 findings.

6

7 **2. Hemi-spherical craters**

8 In this section, we use experimental, computational, and analytical approaches to study isolated hemi-
 9 spherical craters underwater. The computational framework established in this section will be applicable to
 10 more general classes of isolated craters.

11 **2.1 Problem description**

12 Consider a specimen containing a hemi-spherical crater with radius a at its bottom (Fig. 1a). The
 13 specimen rests on a fixed rigid platform, both submerged in liquid. The liquid inside the crater is the same
 14 as in the ambient, and is characterized by the initial volume V_0 , the total number of molecules N_0 , and the
 15 hydrostatic pressure p_0 which can be written as

$$16 \quad p_0 = p_a + wh$$

17 where p_a is the atmospheric pressure, w is the specific weight of the liquid, and h is the distance from the
 18 cratered surface to the liquid surface, a.k.a. liquid depth. The projected area of the undeformed crater is
 19 denoted by A_0 .

20 Under such settings, the suction effect can be realized in the following two sequential stages:

- 21 1. The specimen is compressed, so that some liquid is squeezed out of the crater; at the end of this
 22 stage, the remaining liquid in the crater is characterized by the triplet (p_1, V_1, N_1) (Fig. 1b).
- 23 2. The specimen is unloaded, so that the crater springs back partially. The elastic recovery of the
 24 specimen reduces the pressure of the liquid inside the crater, generating the suction effect. At the
 25 end of this stage, the liquid in the crater is characterized by the triplet (p_2, N_2, V_2) (Fig. 1c).
 26 Accordingly, the negative pressure generated is $\Delta p = p_2 - p_0$.

27 We are interested in the suction force upon full unloading which is defined as

$$F = -\Delta p A_2 \quad (1)$$

1 where A_2 is the projected area of the crater at the end of Stage 2. A complete analysis of the two-stage
 2 process requires one to model the liquid flow. In this paper, we avoid this task by adopting the following
 3 assumptions:

- 4 1. The liquid flows freely out of the crater upon loading, so that $p_1 = p_0$.
- 5 2. No liquid exchange takes place upon unloading, so that $N_1 = N_2$.
- 6 3. The entire process is isothermal and the liquid is incompressible, so that $V_1 = V_2$.

7 The first assumption that the liquid can flow out freely when compressed is inspired by prior works on
 8 thin-walled suction cups³³⁻³⁵. In these models³³⁻³⁵, analytical relationship between preload and suction-cup
 9 deformation has been obtained by neglecting gas or liquid resistance during compression. As for the second
 10 assumption that there is no leakage during unloading, it is consistent with experimental observations for
 11 thin-walled suction cups³³⁻³⁵ as well as surface craters⁴⁷. The third assumption of incompressible fluid is
 12 widely adopted for many liquids. With these three assumptions, the dynamics of liquid flow is regarded as
 13 a sequence of static equilibrium states. Consequently, it becomes sufficient to analyze the two-stage process
 14 in the context of solid mechanics, as explained in Section 2.3.

15 One must be aware that our first assumption is only valid when there is finite amount of liquid left
 16 inside the crater at Stage 1. When the crater is fully closed, i.e. when all the liquid is squeezed out of the
 17 crater, complete vacuum is achieved inside the crater. As a result, the negative pressure is simply $-\Delta p = p_a$
 18 $+wh$, and will be maintained throughout the unloading process (Stage 2) if no backflow is allowed. The
 19 third assumption would break down once there is significant vaporization inside the crater, which occurs
 20 when the liquid pressure drops close to the saturated vapor pressure of this liquid. These extreme situations
 21 are elusive in the current model but we will offer in-depth discussions for them in Section 2.4.

22 In the remainder of Section 2, we describe an experimental setup designed to conform to the adopted
 23 assumptions and measure the suction force. Further, we show that the experimental results can be predicted
 24 using nonlinear elasticity theory up to moderate deformation. That means neglecting the dynamics of liquid
 25 flow appears to be a good assumption. In contrast, linear elasticity theory fails to predict the suction force
 26 under, important for practical purposes, moderate preloads.

27

28 **2.2 Experiments**

1 The experimental setup was designed so that it realized the two-stage process under conditions that
2 well represent the adopted assumptions. First, polydimethylsiloxane (PDMS, Sylgard 184 Dow Corning)
3 with the base-to-curing-agent mass ratio equal to 30:1 was cured at 70°C for 12 hours to mold a cylindrical
4 specimen with diameter 25.40 mm and height 35.13 mm. A hemi-spherical crater of diameter 12.70 mm
5 was placed at the center of a circular face. The material constitutive behavior was measured to fit an
6 incompressible neo-Hookean model with shear modulus $\mu = 47.3$ kPa in our recent work⁵². Note that a
7 hydrostatic pressure will not induce any deformation in an incompressible polymer⁵⁴. During the entire
8 loading-unloading process (Fig. 1), as long as there is still incompressible fluid inside the crater, the whole
9 specimen would be subjected to a hydrostatic pressure $p_0 = p_a + wh$. On top of that, a negative pressure is
10 applied inside the crater during the unloading stage. Superimposing an imaginary hydrostatic tensile stress
11 $\sigma = wh$ to the whole specimen changes its hydrostatic stress state to $p_0 - \sigma = p_a$, yet introducing no
12 deformation due to its incompressibility. In other words, the specimens' response is independent of the
13 liquid depth h , yielding a depth-independent suction effect. However, this argument breaks down when the
14 incompressibility of the filling liquid no longer holds. For example, when the liquid is fully squeezed out
15 at the end of Stage 1 or when the liquid starts to vaporize. Both situations will be discussed in detail in
16 Section 2.4. Neglecting the two extreme cases at this point, we can simply fill the crater with incompressible
17 fluid and perform the experiments in air at the sea level, i.e., $h = 0$ and $p_0 = p_a$ in our experiment.

18 To realize experimental conditions that well represent the adopted assumptions, we built a special
19 platform as illustrated by the schematic in Fig. 2a. The corresponding photograph is offered in Fig. 2b. The
20 cratered specimen was compressed against a stiff acrylic platform. At the center of the platform, we drilled
21 a ventilation hole with a diameter of 0.8 mm, which was used for releasing and trapping liquid in the crater.
22 During Stage 1 (loading), consistent with the first assumption, the vent hole was kept open. During Stage
23 2 (unloading), consistent with the second assumption, the hole was sealed. Without the vent hole, we
24 noticed that there was resistance against liquid flowing out. Therefore, future studies should be carried out
25 accounting for such resistance.

26 Direct measurements of the suction force upon unloading are difficult. Therefore we performed the
27 loading-unloading-pulling-off experiments on the specimens and measured the pull-off force rather than
28 the suction force. These data will be used to extract the suction force. We conducted a series of uniaxial
29 compression and retraction tests using a Dynamic Mechanical Analyzer (DMA) (RSA-G2, TA Instruments)
30 and a Mechanical Testing System (MTS Servohydraulic load frame with Instron 8500R controller). The
31 load cell of the DMA has good resolution (10 μ N) but limited range (up to 35 N), whereas the load cell in
32 the MTS (Omega LCHD-50) has sufficient range (222 N) but lower resolution (0.22 N). Thus, experiments
33 with loading forces greater than 35 N were performed with the MTS, while the rest were done using the

1 DMA. In both testing systems, the top and bottom surfaces of the specimen were lubricated by performance
 2 oil (Fellowes Powershred Performance Shredder Oil) such that the specimen was free of friction and loaded
 3 under uniaxial stress. The loading velocity was set at 3 mm/min, which corresponds to a nominal strain rate
 4 of $1.42 \times 10^{-3} \text{ s}^{-1}$, so that the deformation was dominated by rubber elasticity.

5 To measure the pull-off force, Stage 2 involved not only unloading but also retraction. That is, during
 6 Stage 1, the specimen was stretched beyond the unloading point, until the cratered surface was pulled off
 7 from the platform. This pull-off force is denoted as F' . To extract the suction force, we performed the same
 8 loading-unloading experiments with the vent hole open throughout the test and the collected pull-off force
 9 is denoted as F'' . Representative load-displacement curves for both cases are plotted in Figs. 2c and 2d
 10 where we identify the loading, unloading, and retraction stages, as well as the pull-off forces. Note that the
 11 two sets of data are qualitatively similar. Nevertheless, quantitative differences are significant enough to
 12 reveal the suction effect. For comparison purpose, the pull-off force F' was also measured when the crater
 13 was filled with air.

14 The experimentally collected pull-off force F' can be thought as a resultant force of the adhesion
 15 strength over the specimen/platform interface and the suction force over the crater, whereas F'' only consists
 16 of the interface adhesion. Thus, the difference in value

$$F = F' - F'' \quad (2)$$

17 produces the suction force inside the crater at pull-off as illustrated by the free body diagram in Fig. 2e.

18 In Fig. 2f, the suction force given by Eq. (2) is plotted against the preload ϵ , which is defined as

$$19 \quad \epsilon = -\Delta L/L$$

20 where L is the undeformed specimen length and ΔL is the total shortening at the end of Stage 1. Results for
 21 liquid-filled craters are plotted in red, and air-filled craters are in blue. Solid dots denote results measured
 22 by the DMA while hollow dots were measured by the MTS. Note that DMA results were limited to
 23 $0 \leq \epsilon \leq 0.32$, due to the force limitation of the DMA. At $\epsilon \approx 0.32$, we measured the pull-off forces by both
 24 DMA and MTS. The results are in good agreement, which mutually verified each other. The plot suggests
 25 that for the same specimen, higher suction force can be generated with higher preloads. At the same preload,
 26 the suction force is stronger in liquid-filled craters than the air-filled ones.

27

28 2.3 Simulations

1 Following the framework developed in our previous study⁵², we can model the specimen to be
 2 incompressible neo-Hookean material with shear modulus $\mu = 47.3$ kPa. Further, to simplify the analysis,
 3 we applied axisymmetry and the specimen/substrate interface was assumed to be frictionless (Fig. 3a). Also
 4 we neglected any surface tension effects simply because

$$\frac{\gamma}{a\mu} \approx \frac{2 \times 10^{-2} \text{N/m}}{(10^{-2} \text{ m}) \times (4 \times 10^4 \text{N/m}^2)} = 5 \times 10^{-5} \ll 1$$

5 where γ is the surface tension of PDMS⁵⁵. We have considered the effects of surface tension only when the
 6 crater size is sufficiently small⁵³. If we assume the liquid inside the crater is incompressible and there is no
 7 liquid exchange during Stage 2, it means that there should be no volume change during Stage 2. As a result,
 8 the negative pressure generated at the end of Stage 2 should be fully controlled by the crater volume at the
 9 end of Stage 1, which is determined by the preload.

10 We used nonlinear finite element simulations to compute the relationship between the suction force
 11 (Eq. (1)) and the preload ϵ . All simulations were conducted using ABAQUS Version 6.14. We built an
 12 axisymmetric model with frictionless contact at the bottom and uniform compressive displacement on the
 13 top. The finite element model with mesh formed by CAX4H elements is displayed in Fig. 3a. This mesh
 14 was selected using basic convergence tests. We used the option *FLUID CAVITY which is ideal for
 15 modeling both stages of the liquid-solid interactions.

16 In simulations, during unloading, liquid-filled craters recover differently from air-filled craters. The
 17 deformation snapshots of liquid- and air-filled craters are displayed in Fig. 3b. The first and last panels in
 18 each sequence are the initial (before loading) and final (end of unloading) configurations, respectively. The
 19 third panels correspond to the end of loading (Stage 1) with $\epsilon = 0.35$, and the rest are intermediate states.
 20 A Supplementary Movie is provided which allows one to visualize the deformation process. At the end of
 21 the unloading (Stage 2), the finite element results indicate that the air-filled crater maintains the spherical
 22 symmetry, whereas the liquid-filled crater doesn't. Further comparisons of air-filled craters and liquid-filled
 23 craters are given in Section 2.4.

24 **2.4 Results**

25 In this section, we first examine the difference between air-filled craters and liquid-filled craters, and
 26 explicitly discuss the effect of the depth of water. We will then compare the experimental and simulation
 27 results for both cases. In addition, we present linear analysis results of this problem based on Eshelby's
 28 formalism⁵⁶.

1 Still considering hemi-spherical craters with $\mu = 47.3$ kPa, finite element simulation results for
 2 different parameters at the end of unloading as functions of ϵ are plotted in Fig. 4: (a) normalized pressure
 3 drop $-\Delta p/p_a$, which is positive as Δp is the negative pressure, (b) phase diagram of pressure drop as a
 4 function of liquid depth h and preload ϵ , (c) normalized projected area A_2/A_0 , and (d) normalized suction
 5 force, defined as

$$\tilde{F} = -\Delta p A_2 / (p_a A_0) \quad (3)$$

6 Full closure of the hemi-spherical craters happens at $\epsilon_f = 0.47$, which is independent of the type of the
 7 filling and denoted by vertical magenta dashed lines in all plots. After full closure, complete vacuum, i.e., p_2
 8 $= 0$ is achieved for craters of both fillings such that further compression will no longer increase suction.
 9 Therefore, the maximum preload was chosen as $\epsilon = 0.5$ in all finite element simulations.

10 Figure 4a clearly shows craters of both fillings experience an increase in pressure drop with growing
 11 preload ϵ , whereas the liquid-filled craters exhibit faster increase due to the stronger constraint on the
 12 polymer matrix under volume conservation, i.e., $V_1 = V_2$, compared with ideal gas relation $p_1 V_1 = p_2 V_2$. It
 13 can be safely predicted that both craters should achieve vacuum when fully closed, i.e., $p_2 = 0$, such that
 14 the pressure drop for air-filled crater and liquid-filled crater should be $-\Delta p = p_a$ and $-\Delta p = p_a + wh$,
 15 respectively. As shown by the blue curve in Fig. 4a, air-filled craters indeed reach $-\Delta p = p_a$ at full closure,
 16 which is consistent with our prediction. However, liquid-filled craters show a plateau of pressure drop of
 17 $-\Delta p = 2.2 p_a$ at full closure, which is contradictory to the fact that pressure drop is dependent on liquid
 18 depth at full closure, i.e., $-\Delta p = p_a + wh$. This discrepancy results from the assumption of incompressible
 19 fluid behavior which enforces zero crater volume, i.e., $V_2 = 0$, throughout the unloading process in finite
 20 element simulation. Such a rigid constraint of volume conservation $V_2 = V_1 = 0$ at full closure contradicts
 21 with reality, thus the finite element results of $\epsilon > \epsilon_f$ in Fig. 4a (as shown by magenta markers) for liquid-
 22 filled craters are not meaningful. In reality, when the pressure inside the crater approaches the saturated
 23 vapor pressure of the liquid (denoted by p_v), the liquid vaporizes rapidly (e.g., boiling), violating the
 24 assumption of incompressibility. In this case, vaporization models should be incorporated to accurately
 25 predict the negative pressure, which is out of the scope of this paper. The saturated vapor pressure of water
 26 and oil at room temperature is very small compared with atmospheric pressure, e.g., $p_v \approx 2$ kPa for water
 27 and $p_v \approx 0.1$ kPa for the performance oil (99 wt% canola oil) used in our experiment according to the
 28 product sheet. Herein, we simply assume that the liquid vaporizes when the pressure inside the crater drops
 29 to zero, i.e., when $p_2 = 0$ and $-\Delta p = p_a + wh$. The vaporization consideration actually sets an upper bound
 30 for the validity of the finite element results shown in Fig. 4a. For example, consider a hemisphere-cratered

1 specimen filled with liquid at sea level, i.e., $h = 0$, and the vaporization occurs when $-\Delta p = p_a$. A
 2 horizontal line of $-\Delta p = p_a$ (black dashed line) intersects with the curve of $-\Delta p/p_a(\epsilon)$, showing a critical
 3 preload $\epsilon_v^0 = 0.35$. When the preload is smaller than ϵ_v^0 , we simply assume that no vaporization will happen
 4 as the pressure inside the crater is still positive, i.e., $p_2 > 0$. Therefore, finite element results below ϵ_v^0 are
 5 valid while those above ϵ_v^0 are not. The critical preload for vaporization ϵ_v depends on the liquid depth h in
 6 that the pressure drop simply equals to the ambient pressure when vaporization occurs, i.e., $-\Delta p = p_a + wh$.
 7 If we simply fit the finite elements results of liquid-filled craters in Fig. 4a by using $-\Delta p/p_a = f(\epsilon)$ for 0
 8 $\leq \epsilon \leq \epsilon_f$ (red curve), ϵ_v can be obtained by solving the equation $f(\epsilon_v) = 1 + wh/p_a$ for a given liquid
 9 depth h . When $\epsilon < \epsilon_v$, i.e. when $f(\epsilon) < f(\epsilon_v) = 1 + wh/p_a$, no vaporization would occur. As a result, we
 10 can write the pressure drop as a function of liquid depth h and preload ϵ :

$$-\frac{\Delta p}{p_a}(\epsilon, h) = \begin{cases} f(\epsilon) & 0 \leq \epsilon < \epsilon_v^0, \forall h \\ f(\epsilon) & \epsilon_v^0 \leq \epsilon < \epsilon_f \text{ \& } wh/p_a > f(\epsilon) - 1 \\ \text{Vaporization, no solution} & \epsilon_v^0 \leq \epsilon < \epsilon_f \text{ \& } wh/p_a \leq f(\epsilon) - 1 \\ 1 + wh/p_a & \epsilon \geq \epsilon_f \end{cases} \quad (4)$$

11 Equation (4) can be illustrated by a phase diagram as Fig. 4b where the horizontal axis is the preload ϵ
 12 and the vertical axis is the normalized liquid depth wh/p_a . The solution to pressure drop will be different
 13 in different regimes. The brown regimes are non-vaporizations zones where the pressure drop is simply
 14 characterized by $-\Delta p/p_a = f(\epsilon)$, the red regime is where vaporization would occur, and the cyan regime
 15 represents complete vacuum. When $\epsilon < \epsilon_v^0 = 0.35$, the pressure inside the crater after unloading is always
 16 above zero, i.e., non-vaporization, and the pressure drop is given by $-\Delta p/p_a = f(\epsilon)$ which is independent
 17 of liquid depth h as the hydrostatic pressure wh does not deform the incompressible specimen. When $\epsilon_v^0 \leq \epsilon$
 18 $< \epsilon_f = 0.47$, vaporization occurs when $-\Delta p \geq p_a + wh$, i.e., $wh/p_a \leq -\Delta p/p_a - 1 = f(\epsilon) - 1$, as
 19 highlighted by the red regime. Hence, when $wh/p_a > f(\epsilon) - 1$, no vaporization happens and our finite
 20 element results are useful. Interestingly, according to the finite element results in Fig. 4a, when the preload
 21 approaches ϵ_f , the pressure drop is capped at $-\Delta p/p_a = 2.2$, corresponding to a maximum normalized
 22 liquid depth for vaporization $wh/p_a = 1.2$. It means that for normalized liquid depth higher than 1.2, the
 23 craters will be fully closed prior to the significant vaporization of the liquid. Such a critical liquid depth is
 24 about 12 m for water if we simply take $w \approx 10^4$ N/m³. When $\epsilon \geq \epsilon_f$, the hemispherical crater attains full
 25 closure and realizes complete vacuum, giving rise to $-\Delta p = p_a + wh$, regardless of the flawed finite
 26 element simulation at full closure. Therefore, when the crater is fully closed, craters in deeper waters will
 27 produce higher suction force. We need to point out again that the vaporization discussed in this paper refers

1 to the rapid liquid-to-vapor phase transition, e.g., boiling, rather than the slow evaporation that is always
2 ongoing on the liquid surface.

3 After fully understanding the pressure drop, we are ready to look at the suction force \tilde{F} given in Eq.
4 (3). The projected area A_2 is affected by the instabilities in the craters subjected to large preload. In Fig. 4a,
5 the horizontal dashed green line represents the critical Δp_c , beyond which the hemispherical shape of the
6 crater breaks down upon unloading, irrespective of the filling or the depth of liquid. This critical load $-\Delta p_c$
7 $= 0.83p_a$ is obtained by analyzing the surface instability of a spherical void in an infinitely large block
8 (Appendix A)^{57, 58}. And the corresponding critical preload ϵ_c is 0.33 and 0.43 for liquid- and air-filled
9 craters, respectively.

10 As observed in finite element simulation results in Fig. 3b, once instability happens upon unloading,
11 the partially recovered crater shows shallower but wider profile, giving rise to increased projected area, i.e.
12 larger A_2 . This explains the slight increase of the A_2/A_0 at ϵ_c for both liquid-filled and air-filled craters
13 plotted in Fig. 4c. However, for liquid-filled craters, the instability induced increase in A_2 doesn't last. This
14 is because the volume conservation constraint also gets stronger with increasing preload ϵ and eventually
15 overwhelms other factors, leading to the re-decrease of A_2 , as shown in Fig. 4c. For liquid-filled craters, A_2
16 eventually drops to 0 with fully closed craters due to the volume conservation enforced in the finite element
17 simulation. The increasing Δp and the overall decreasing A_2 together produce an \tilde{F} that varies non-
18 monotonically with ϵ for liquid-filled craters, as plotted in Fig. 4d. But as we discussed before, for liquid-
19 filled craters at sea level, vaporization begins at $\epsilon_v^0 = 0.35$, which is represented by the black dashed lines
20 in Figs. 4c and 4d. Therefore, the finite element results for A_2 and \tilde{F} of liquid filled craters (the red curves)
21 are no longer meaningful beyond the black dashed lines. However, the blue curves for air-filled craters
22 should be valid all the way till full closure, i.e. $\epsilon_f = 0.47$.

23 Comparison of simulation (solid curves) and experimental (circular markers) results for hemi-spherical
24 craters is conducted in Fig. 5a, where the suction force is plotted versus the preload ϵ . Results corresponding
25 to liquid-filled craters are plotted in red, and air-filled craters are in blue for comparison. In the range of
26 $0 \leq \epsilon \leq 0.3$, experimental and simulation results are in good agreement for both types of craters. This
27 validates the theoretical framework we developed and also justifies applying the framework on craters of
28 other shapes under moderate preload. We also calculated the suction force using linear (infinitesimal strain)
29 analysis based on Eshelby's formalism⁵⁶. This approach is possible because of the assumptions that the
30 specimen is large compared with the crater, the interface is frictionless, and the surface tension effects are
31 negligible. Details of this analysis are presented in Appendix B, and the results (dotted curves) are shown

1 in Fig. 5a. It is clear that the linear analysis is valid for small strains, and deviates significantly from the
 2 experimental and simulation results for $\epsilon > 0.1$, and therefore its usefulness is rather limited.

3 Under large preload, especially when the crater reaches full closure, finite element simulation shows
 4 considerable discrepancy from experimental results for both air-filled craters and liquid-filled craters. For
 5 air-filled craters, we recognize that the source of the discrepancy comes from the different definitions of
 6 suction force used in experiments and simulations. In experiments, $F' - F''$ (Eq. (2)) represents the suction
 7 force inside the crater at pull-off, while in simulations, $-\Delta p A_2$ (Eq. (1)) is used to calculate suction force
 8 at the end of unloading, without any retraction. At small to moderate preload, it is fair to argue that the
 9 crater has similar a configuration at pull-off and full unloading, so that

$$F' - F'' \approx -\Delta p A_2 \quad (5)$$

10 is expected. This is true under loading range $0 \leq \epsilon \leq 0.3$ based on the observation from Fig. 5a. However,
 11 this approximation will no longer hold when the crater shapes are very different at pull-off and full
 12 unloading. To verify this hypothesis, we applied experimentally measured retraction strain at pull-off, ϵ_t in
 13 simulation beyond full unloading. Resulted suction forces, $F = -\Delta p' A_2'$, are plotted as solid blue diamonds
 14 in Fig. 5a, where $\Delta p'$ and A_2' represent the finite element results of pressure drop inside the crater and the
 15 projected area of the crater at pull-off, respectively, at the pull-off point. Figure 5b depicts the profiles of
 16 air-filled craters at unloading (blue curve) and pull-off (red curve) and visible difference can be found at
 17 full closure. In Fig. 5a, the good agreement between $F = -\Delta p' A_2'$ (the diamond markers) and $F' - F''$ (the
 18 circular markers) indicates that, for air-filled craters, the discrepancy between the finite element results of
 19 suction force (the solid curve) and the experimentally measured pull-off force (the circular markers) can be
 20 fully explained by the difference in unloading vs. pull-off points. In other words, for air-filled craters, our
 21 finite element simulation is valid all the way up to the preload that fully closes the crater in terms of
 22 predicting the suction force at full unloading before retraction.

23 For liquid-filled craters, finite element results start to deviate from experiments when the preload $\epsilon >$
 24 0.3. In addition to the difference between suction and pull-off forces discussed above, there are other
 25 reasons which are only pertinent to liquid fillings. As we already know, the liquid inside the crater may
 26 undergo liquid-to-vapor phase transition when preload approaches the critical value $\epsilon_v^0 = 0.35$ as
 27 experiments are carried at sea level in air, i.e., $h = 0$. Vaporization would enlarge pressure inside the crater,
 28 thus compromising the suction force and hence the measured pull-off force. Moreover, the critical preload
 29 for vaporization $\epsilon_v^0 = 0.35$ was obtained without considering retraction strain ϵ_t in the simulation while the
 30 experimental results were measured at the pull-off points. Applying retraction strain to the specimen beyond

1 full unloading will further reduce the liquid pressure inside the crater, causing the liquid to vaporize prior
 2 to the critical preload $\epsilon_v^0 = 0.35$. This can explain why deviation between finite element results and
 3 experiments starts after $\epsilon = 0.3$ rather than 0.35. Further discussions regarding the effects of retraction on
 4 vaporization are offered in Section 3. Thus, for liquid-filled craters, the applicability of finite element
 5 simulation under large preload is limited to moderate preload. For the specimens used in this paper, the
 6 deviation between finite element simulation and experiments occurs at $\epsilon \approx 0.3$. One should note that the
 7 deviation may occur at different preload ϵ if the specimens are made of different materials or the crater
 8 shape is different or the specimen is at different depth of liquid.

9 It is also obvious that experimentally, craters with both fillings produced similar suction forces after
 10 full closure, validating our expectation that at full closure, the pressure drop in both types of craters should
 11 equal the ambient pressure at sea level, i.e., $-\Delta p = p_a$.

12 To accurately predict the pull-off force, one needs the traction-separation behavior of the
 13 specimen/platform interface, and the vaporization process of the liquid, which are out of our current focus.
 14 So, for Section 3, we would focus on the study of the suction force given by Eq. (1).

15 **3. Spherical-cap-shaped (SCS) craters**

16 In this section, we extend the experimental and simulation approach established for hemi-spherical craters
 17 to spherical-cap-shaped (SCS) craters that are filled with incompressible fluid. Our objective is to
 18 investigate the effects of crater shape and preload so we fix the material modulus to be $\mu = 47.3$ kPa. In
 19 fact, according to dimensional analysis, the pressure drop and hence the suction force for underwater craters
 20 have to scale with the modulus of the specimen μ as p_a is not relevant except when considering vaporization
 21 or full closure. In this section, however, we will continue to use p_a in the normalization just to be consistent
 22 with Fig. 4, where air-filled craters were compared with liquid-filled ones. Since our analysis is limited to
 23 large specimens, the only dimensionless geometric parameter involved is the crater aspect ratio, i.e. b/a ,
 24 where a is crater base radius and b is the crater height (Fig. 6a). Finite element results of pressure drops as
 25 a function of preload for SCS craters with various aspect ratios ($b/a = 0.1, 0.2, 0.3, 0.4, 0.5, 0.6, 0.7, 0.8,$
 26 0.9 and 1) are plotted in Fig. 6b. For each b/a , the location of the preload of full closure is marked by the
 27 arrow. It is evident that shallower craters reach full closure at smaller preload than the deeper ones.
 28 Particularly, SCS craters with aspect ratio $b/a < 0.5$ reach full closure before $\epsilon_v^0 = 0.35$, meaning that no
 29 vaporization will take place before such craters are fully closed. For SCS craters with aspect ratios
 30 $b/a \geq 0.5$, our simulation result indicates that they have the same critical preload for vaporization, i.e. the
 31 curves all intersect at $\epsilon_v^0 = 0.35$ as evidenced in Fig. 6b. At this moment, we do not have an explanation for

1 this observation. To validate our finite element simulation results for SCS craters with different aspect ratios,
 2 we conducted extra experiments on two SCS craters with aspect ratios $b/a = 0.25$ and 0.5 . To eliminate
 3 the effect of A_0 , the crater base radius $a = 6.35$ mm was fixed in all three specimens. All experiments were
 4 conducted in air with liquid filling at sea level under room temperature. Numerical (curves and diamond
 5 markers) and experimental (circular markers) results of suction forces for SCS craters with
 6 $b/a = 0.25, 0.5$, and 1 are plotted together in Fig. 6c. It is obvious that the simulated suction forces only
 7 agree with measured pull-off forces at small to moderate preload. The shallower the crater, the earlier the
 8 deviation. For craters with $b/a = 0.25, 0.5$ and 1 , the preload at deviation are $\epsilon_d = 0.05, 0.13$ and 0.3 ,
 9 respectively. For hemispherical crater, i.e., $b/a = 1$, towards the end of Section 2.4, this discrepancy was
 10 partially attributed to the possible vaporization when preload approaches $\epsilon_v^0 = 0.35$ (as shown by the black
 11 dashed line in Fig. 6c). However, for craters with $b/a = 0.25$ and 0.5 , no vaporization would occur under
 12 such small preload, i.e., $\epsilon_d = 0.05$ and 0.13 , according to Fig. 6b. Therefore, we hypothesize that the
 13 deviation is due to the difference between simulated suction forces given by Eq. (1) and measured pull-off
 14 forces extracted using Eq. (2). To prove it, we added a retraction stage in finite element simulation where
 15 the applied retraction strain is the same as the pull-off strain in experiments. In this way, we can numerically
 16 obtain the suction force at the pull-off point for craters with $b/a = 0.25$ and 0.5 . Simulated results are
 17 plotted as diamond markers in Fig. 6c, which agree well with the experiments. This agreement validates
 18 our hypothesis and implies that our finite element simulated suction forces (the solid curves), which are
 19 defined to be the attachment force at the end of unloading and before retraction, are valid. But adding
 20 retraction strain for fluid-filled craters should be conducted with caution because retraction strain would
 21 further reduce the hydrostatic pressure in the liquid, expediting vaporization. For instance, for craters with
 22 $b/a = 0.5$ under preload $\epsilon = 0.29$, no vaporization happens at the end of unloading. However, after
 23 applying retraction, the pressure drop further increases beyond 1, which means although vaporization does
 24 not take place the end of unloading, it could happen at the pull-off point. Therefore, the critical preload for
 25 vaporization at pull-off, ϵ_v^{p0} , is smaller than that at the end of unloading, ϵ_v . We use blue dashed line to
 26 represent ϵ_v^{p0} in Fig. 6c. Left to this line, finite element simulated suction forces at the pull-off point (blue
 27 diamonds) and experimentally measured pull-off forces (blue dots) match perfectly. Right to this line,
 28 evaporation kicks in so finite element simulation becomes useless. For craters with $b/a = 0.25$, the
 29 maximum preload used in experiment was 0.2 , by which no vaporization would occur according to the
 30 finite element results at the pull-off point. Therefore, the modified finite element results (yellow diamonds)
 31 can fully capture the measured pull-off forces (yellow dots). From such exercise, we learned that as long as
 32 the crater is not fully closed and the liquid inside remains as incompressible, i.e. no vaporization, the
 33 discrepancy between the finite element curves and experimental dots in Fig. 6c purely stems from the

1 different definitions of suction force, rather than the numerical approach itself. Therefore, it is reasonable
 2 to believe that the finite element curves before the black dashed curve ($\epsilon_v^0 = 0.35$) are able to capture the
 3 true suction forces at the end of unloading.

4 To summarize the effects of preload and aspect ratio on suction forces, we offer a contour plot for the
 5 normalized suction force \tilde{F} at full unloading (Eq. (3)) in Fig. 6d. First, the white regime represents vacuum
 6 due to full closure. If the crater reaches vacuum, the pressure drop is simply given by $-\Delta p = p_a + \rho h$, which
 7 is obviously dependent on the depth of liquid, h . When $h = 0$ and the crater reaches vacuum, our previous
 8 results for air-filled craters at full closure (Fig. 6b in ref⁵²) are applicable. Second, before the crater is fully
 9 closed, the liquid vaporizes when the preload is beyond $\epsilon_v^0 = 0.35$ when $h = 0$ (shown by the black dashed
 10 curve). Note that ϵ_v changes with h and the dependence is shown in Fig. 4b. Our simulation results beyond
 11 ϵ_v are not meaningful due to liquid vaporization. Third, below ϵ_v is the non-vaporization zone, where our
 12 numerical results have been validated by experiments as discussed in Fig. 6c and such results are
 13 independent of h as discussed in Section 2.4. It is clear that the suction force has a non-monotonic
 14 dependence on the aspect ratio of the craters. The highest suction force $\tilde{F} = 0.69$ can be generated by a SCS
 15 crater with $b/a = 0.8$ under preload $\epsilon \approx 0.34$, as highlighted by the white star in Fig. 6d.

16

17 4. Conclusion

18 In this paper, we try to elucidate adhesion generated by cratered surface underwater or more generally,
 19 immersed in incompressible fluid. Such enhanced adhesion is purely enabled by suction force due to
 20 pressure difference between the crater and the ambient, thus is reversible. We restricted ourselves to isolated
 21 macroscopic SCS craters, for which surface tension and other microscopic mechanisms were assumed to
 22 be negligible. The restriction to SCS craters is dictated by manufacturing considerations, but of course one
 23 can consider other shapes. Both experimental and simulation results focused on specimens resting on
 24 frictionless substrates with small vent holes. Clearly, friction would weaken the suction effect as it requires
 25 large force to close the crater. Therefore, reducing friction should be desirable for all practical purposes.
 26 Vent holes are necessary to satisfy our assumption of zero resistance to fluid flow. In reality, nonzero
 27 resistance may exist and hence would further weaken the suction effects. Under such idealized assumptions,
 28 our key findings are summarized as follows:

- 29 • As long as the specimen is immersed in incompressible fluid and the fluid inside the crater does
 30 not vaporize or fully disappear, the suction forces generated are independent of the depth of the

1 liquid and can be confidently predicted by the framework established in this paper even under large
2 preload.

3 • In this case, suction force measurement for underwater crater can be simply carried out in air with
4 liquid filled in the crater.

5 • In this case, suction force produced by underwater crater scales with the modulus of the polymer
6 material.

7 • In this case, for specimen of $\mu = 47.3$ kPa examined in this paper, with the same crater geometry,
8 underwater craters are capable of producing stronger suction force than craters in air.

9 • In this case, for specimen of $\mu = 47.3$ kPa examined in this paper with liquid filling, the largest
10 suction forces $\tilde{F} = 0.69$ can be generated by a SCS crater with $b/a = 0.8$ under preload $\epsilon \approx 0.34$.

11 • If the crater is fully closed during loading, vacuum is generated in the crater and the resulting
12 suction force should be independent of the filler but dependent on the depth of the liquid.

13 • The depth of the liquid and the preload together dictate when the liquid inside the crater would
14 vaporize. When $wh/p_a > 1.2$, the liquid would never vaporize at the end of unloading even up to
15 full closure.

16

17

18 **Acknowledgements**

19 Authors acknowledge the support from the National Science Foundation (NSF) Division of Civil,
20 Mechanical and Manufacturing Innovation (CMMI) award (Grant No. 1663551). Shutao Qiao and Liu
21 Wang acknowledge the Warren A. and Alice L. Meyer endowed graduate fellowship awarded by the
22 Cockrell School of Engineering at the University of Texas at Austin. Kyoung-Ho Ha acknowledges the
23 Philip C. and Linda L. Lewis Foundation Graduate Fellowship in Mechanical Engineering at the University
24 of Texas at Austin.

25

1 Appendix A

2 On the surface of the spherical void in an infinitely large block, traction $-\Delta p$ is exerted in normal
 3 direction, and one has principal stretches λ_r , λ_θ and λ_ϕ on the surface. Before the spherical symmetry breaks
 4 down, for incompressible Neo-Hookean block with shear modulus μ , Δp can be written as

$$-\frac{\Delta p}{\mu} = \frac{4\lambda_\theta^3 + 1}{2\lambda_\theta^4} - \frac{5}{2} \quad (\text{A1})$$

5 The critical condition of a surface crease setting in is given as⁵⁸

$$\frac{\lambda_r}{\lambda_\theta} = 2.4 \quad (\text{A2})$$

6 Considering the spherical symmetry as well as incompressibility of the block material, before crease sets
 7 in, the principal stretches follow

$$\lambda_\theta = \lambda_\phi = \frac{1}{\sqrt{\lambda_r}} \quad (\text{A3})$$

8 Combining Eqs. (A1) - (A3) leads to the critical load $\Delta p_c = -1.78\mu$, and $-\Delta p_c/p_a = 0.83$ when
 9 $\mu = 47.3$ kPa.

10 Appendix B

11 In this appendix, we derive an analytical solution of classical linear elasticity theory for the pressure drop
 12 of an underwater isolated hemi-spherical crater in a semi-infinite specimen under remote compressive load.
 13 We take advantage of the assumption that the contact between the specimen and the substrate is frictionless.
 14 This allows us to replace the problem for semi-infinite specimen containing a hemi-spherical crater with an
 15 infinite specimen containing a spherical cavity. This problem is straightforward to analyze using Eshelby's
 16 formulism⁵⁶.

17 According to Eq. (2), we need to calculate V_1 and V_2 . To compute ΔV_1 , we subject the infinite specimen
 18 to remote uniaxial compressive strain ϵ . For this case, the specimen has Poisson's ratio equal to 0.5 such
 19 that Eshelby's formulism yields

$$\Delta V_1 = -\frac{3}{4}\epsilon V_0. \quad (\text{B1})$$

1 To compute ΔV_2 , we subject the cavity to the surface traction

$$2 \quad \mathbf{t} = (p_a - p_2)\mathbf{n} = -\Delta p \mathbf{n}$$

3 where \mathbf{n} is the outward normal. As far as ΔV_2 is concerned, this problem is equivalent to the superposition
 4 of two problems. In the first problem, the specimen is uniformly loaded by $-\Delta p$ on both cavity and remote
 5 surfaces. In the second problem, the cavity surface is traction-free and the remote surface is subjected to Δ
 6 p . As a result, we obtain

$$\Delta V_2 = \frac{3}{4} \frac{\Delta p}{\mu} V_0. \quad (\text{B2})$$

7 Since the fluid in the cavity is incompressible and there is no fluid exchange during unloading, we have

$$\Delta V_1 = \Delta V_2. \quad (\text{B3})$$

8 Combing Eqns. (A1) ~ (A3), one obtains the pressure drop in the crater upon unloading is

$$\Delta p = -\epsilon \mu. \quad (\text{B4})$$

9 Note that in our previous work⁵², when the crater is filled with ideal gas, the pressure drop in the crater
 10 upon unloading is

$$\Delta p = -\frac{1}{2} \left[\left(1 + \frac{4\mu}{3p_a} \right) - \sqrt{\left(1 + \frac{4\mu}{3p_a} \right)^2 - 8(1-\nu) \frac{\mu}{p_a} \epsilon} \right] p_a. \quad (\text{B5})$$

11

1 Reference

- 2 1. C. Menon, M. Murphy and M. Sitti, 2004.
- 3 2. H. Kim, D. Kim, H. Yang, K. Lee, K. Seo, D. Chang and J. Kim, *J Mech Sci Technol*, 2008, **22**, 1490-
- 4 1498.
- 5 3. S. Seo, J. Lee, K.-S. Kim, K. H. Ko, J. H. Lee and J. Lee, *ACS applied materials & interfaces*, 2014, **6**,
- 6 1345-1350.
- 7 4. W.-Y. Chang, Y. Wu and Y.-C. Chung, *Nano letters*, 2014, **14**, 1546-1550.
- 8 5. H. Lee, D. S. Um, Y. Lee, S. Lim, H. j. Kim and H. Ko, *Advanced Materials*, 2016, **28**, 7457-7465.
- 9 6. Y.-C. Chen and H. Yang, *ACS nano*, 2017, **11**, 5332-5338.
- 10 7. M. K. Choi, O. K. Park, C. Choi, S. Qiao, R. Ghaffari, J. Kim, D. J. Lee, M. Kim, W. Hyun, S. J. Kim, H.
- 11 J. Hwang, S.-H. Kwon, T. Hyeon, N. Lu and D.-H. Kim, *Advanced Healthcare Materials*, 2016, **5**, 80-
- 12 87.
- 13 8. M. K. Kwak, H. E. Jeong and K. Y. Suh, *Advanced Materials*, 2011, **23**, 3949-3953.
- 14 9. M. Cui, S. Ren, S. Wei, C. Sun and C. Zhong, *APL Materials*, 2017, **5**, 116102.
- 15 10. J. Li, A. Celiz, J. Yang, Q. Yang, I. Wamala, W. Whyte, B. Seo, N. Vasilyev, J. Vlassak and Z. Suo,
- 16 *Science*, 2017, **357**, 378-381.
- 17 11. Y. Zhao, Y. Wu, L. Wang, M. Zhang, X. Chen, M. Liu, J. Fan, J. Liu, F. Zhou and Z. Wang, *Nature*
- 18 *communications*, 2017, **8**, 2218.
- 19 12. K. Autumn, Y. A. Liang, S. T. Hsieh, W. Zesch, W. P. Chan, T. W. Kenny, R. Fearing and R. J. Full,
- 20 *Nature*, 2000, **405**, 681-685.
- 21 13. D. J. Irschick, C. C. Austin, K. Petren, R. N. Fisher, J. B. Losos and O. Ellers, *Biological journal of the*
- 22 *Linnean Society*, 1996, **59**, 21-35.
- 23 14. K. Autumn, M. Sitti, Y. A. Liang, A. M. Peattie, W. R. Hansen, S. Sponberg, T. W. Kenny, R. Fearing,
- 24 J. N. Israelachvili and R. J. Full, *Proceedings of the National Academy of Sciences*, 2002, **99**, 12252-
- 25 12256.
- 26 15. E. Arzt, S. Gorb and R. Spolenak, *Proceedings of the National Academy of Sciences*, 2003, **100**,
- 27 10603-10606.
- 28 16. R. Spolenak, S. Gorb, H. Gao and E. Arzt, 2005.
- 29 17. M. P. Murphy, S. Kim and M. Sitti, *ACS applied materials & interfaces*, 2009, **1**, 849-855.
- 30 18. K. Jin, Y. Tian, J. S. Erickson, J. Puthoff, K. Autumn and N. S. Pesika, *Langmuir*, 2012, **28**, 5737-5742.
- 31 19. H. Lee, B. P. Lee and P. B. Messersmith, *Nature*, 2007, **448**, 338-341.
- 32 20. M. D. Bartlett, A. B. Croll, D. R. King, B. M. Paret, D. J. Irschick and A. J. Crosby, *Advanced Materials*,
- 33 2012, **24**, 1078-1083.
- 34 21. M. P. Murphy, B. Aksak and M. Sitti, *Small*, 2009, **5**, 170-175.
- 35 22. Y. Mengüç, S. Y. Yang, S. Kim, J. A. Rogers and M. Sitti, *Advanced Functional Materials*, 2012, **22**,
- 36 1246-1254.
- 37 23. S. Chary, J. Tamelier and K. Turner, *Smart Materials and Structures*, 2013, **22**, 025013.
- 38 24. S. Buhl, C. Greiner, A. d. Campo and E. Arzt, *International Journal of Materials Research*, 2009,
- 39 **100**, 1119-1126.
- 40 25. N. Cadirov, J. A. Booth, K. L. Turner and J. N. Israelachvili, *ACS applied materials & interfaces*, 2017,
- 41 **9**, 14497-14505.
- 42 26. N. S. Pesika, H. Zeng, K. Kristiansen, B. Zhao, Y. Tian, K. Autumn and J. Israelachvili, *Journal of*
- 43 *Physics: Condensed Matter*, 2009, **21**, 464132.
- 44 27. W. M. Kier and A. M. Smith, *The Biological Bulletin*, 1990, **178**, 126-136.
- 45 28. W. M. Kier and A. M. Smith, *Integrative and Comparative Biology*, 2002, **42**, 1146-1153.
- 46 29. F. Tramacere, L. Beccai, M. Kuba, A. Gozzi, A. Bifone and B. Mazzolai, 2013.

- 1 30. D. K. Wainwright, T. Kleinteich, A. Kleinteich, S. N. Gorb and A. P. Summers, *Biology letters*, 2013,
2 9, 20130234.
- 3 31. A. M. Smith, *Journal of Experimental Biology*, 1991, **157**, 257-271.
- 4 32. A. Smith, *Journal of Experimental Biology*, 1996, **199**, 949-958.
- 5 33. L. Afferrante, G. Carbone, G. Demelio and N. Pugno, *Tribology Letters*, 2013, **52**, 439-447.
- 6 34. D. Ge, T. Matsuno, Y. Sun, C. Ren, Y. Tang and S. Ma, *Vacuum*, 2015, **116**, 13-20.
- 7 35. J. Liu, K. Tanaka, L. Bao and I. Yamaura, *Vacuum*, 2006, **80**, 593-598.
- 8 36. A. Del Campo, C. Greiner and E. Arzt, *Langmuir*, 2007, **23**, 10235-10243.
- 9 37. A. del Campo, C. Greiner, I. Álvarez and E. Arzt, *Advanced Materials*, 2007, **19**, 1973-1977.
- 10 38. S. C. Fischer, K. Groß, O. Torrents Abad, M. M. Becker, E. Park, R. Hensel and E. Arzt, *Advanced*
11 *Materials Interfaces*, 2017, **4**, 1700292.
- 12 39. S. Baik, J. Kim, H. J. Lee, T. H. Lee and C. Pang, *Advanced Science*, 2018, 1800100.
- 13 40. L. Heepe, M. Varenberg, Y. Itovich and S. N. Gorb, *Journal of the Royal Society, Interface*, 2011, **8**,
14 585-589.
- 15 41. H. Gao and H. Yao, *Proceedings of the National Academy of Sciences of the United States of*
16 *America*, 2004, **101**, 7851-7856.
- 17 42. A. Del Campo and E. Arzt, *Macromolecular bioscience*, 2007, **7**, 118-127.
- 18 43. E. P. Chan, C. Greiner, E. Arzt and A. J. Crosby, *MRS bulletin*, 2007, **32**, 496-503.
- 19 44. C. Greiner, A. D. Campo and E. Arzt, *Langmuir*, 2007, **23**, 3495-3502.
- 20 45. T. Kim, J. Park, J. Sohn, D. Cho and S. Jeon, *ACS nano*, 2016, **10**, 4770-4778.
- 21 46. H. E. Jeong and K. Y. Suh, *Nano Today*, 2009, **4**, 335-346.
- 22 47. S. Baik, D. W. Kim, Y. Park, T.-J. Lee, S. Ho Bhang and C. Pang, *Nature*, 2017, **546**, 396-400.
- 23 48. S. Akerboom, J. Appel, D. Labonte, W. Federle, J. Sprakel and M. Kamperman, *Journal of the Royal*
24 *Society, Interface*, 2015, **12**, 20141061.
- 25 49. G. Nanni, D. Fragouli, L. Ceseracciu and A. Athanassiou, *Applied Surface Science*, 2015, **326**, 145-
26 150.
- 27 50. F. Tramacere, N. M. Pugno, M. J. Kuba and B. Mazzolai, *Interface focus*, 2015, **5**, 20140050.
- 28 51. A. Majumder, A. Sharma and A. Ghatak, *Langmuir*, 2009, **26**, 521-525.
- 29 52. S. Qiao, L. Wang, H. Jeong, G. J. Rodin and N. Lu, *Journal of The Royal Society Interface*, 2017, **14**,
30 20170377.
- 31 53. L. Wang, S. Qiao and N. Lu, *Extreme Mechanics Letters*, 2017, **15**, 130-138.
- 32 54. J. Zimmermann and M. Stommel, *Archive of Applied Mechanics*, 2013, **83**, 293-302.
- 33 55. J. Brandrup, E. H. Immergut, E. A. Grulke, A. Abe and D. R. Bloch, *Polymer handbook*, Wiley New
34 York etc, 1989.
- 35 56. J. D. Eshelby, *Proceedings of the Royal Society of London. Series A. Mathematical and Physical*
36 *Sciences*, 1957, **241**, 376-396.
- 37 57. S. Cai, K. Bertoldi, H. Wang and Z. Suo, *Soft Matter*, 2010, **6**, 5770-5777.
- 38 58. W. Hong, X. Zhao and Z. Suo, *Applied Physics Letters*, 2009, **95**, 111901.

39

1 **Figure Captions**

2 Fig. 1 Schematics for the loading-unloading cycle that produces suction force underwater: (a) A specimen
3 with an isolated hemi-spherical crater of radius a resting on the flat bottom of a tank filled with liquid
4 (blue); (b) The specimen is preloaded in compression and the liquid is squeezed out of the crater; (c) The
5 preload is released, and the crater springs back, resulting in pressure drop in the crater. The symbols p , V ,
6 A and N denote the pressure, volume, projected area, and number of liquid molecules inside the crater at
7 each state.

8 Fig. 2 A schematic (a) and a photograph (b) of the experimental setup. The small ventilation hole drilled in
9 the bottom platform is open during loading and closed during unloading. Load-displacement curves with
10 vent hole open (c) and closed (d) during unloading. Peak compressive strain was 10%. Loading, unloading,
11 retraction stages, and the pull-off points are identified. (e) A schematic of the free body diagram of a
12 specimen at pull-off. (f) Comparisons of experimentally measured suction forces ($F' - F''$) of air-filled (blue
13 markers) and liquid-filled (red markers) craters. Data obtained by DMA are represented by solid dots and
14 MTS by hollow circles.

15 Fig. 3 (a) A finite element mesh for an axisymmetric crater model. (b) Two deformation sequences of
16 specimens in a loading-unloading test with different fillings: top row for air-filled crater and bottom row
17 for liquid-filled crater.

18 Fig. 4 End results of the loading-unloading test are computed and plotted as functions of the preload ϵ : (a)
19 normalized pressure drop $-\Delta p/p_a$, (b) phase diagram of pressure drop as a function of liquid depth h and
20 preload ϵ , (c) normalized projected area A_2/A_0 , and (d) normalized suction force $\tilde{F} = -\Delta p A_2/(p_0 A_0)$.
21 Craters filled with incompressible fluid are represented by circular markers and ideal gas by triangular
22 markers.

23 Fig. 5 (a) Comparisons of suction forces obtained by experimental measurements (circular markers),
24 analytical modeling (dashed curves) and finite element simulation (solid curves and diamond markers).
25 Craters filled with incompressible fluid are represented by red ($0 \leq \epsilon < \epsilon_f$), magenta ($\epsilon_f \leq \epsilon < 0.5$) and
26 ideal gas by blue. (b) Profiles of air-filled craters at undeformed (black dashed curve), full unloading (blue
27 curve), and pull-off (red curve) conditions.

28 Fig. 6 (a) Schematics of spherical-cap-shaped (SCS) crater. (b) Finite element results of pressure drop as a
29 function of preload for various SCS craters. Arrows indicate full closure point. (c) Suction force as a
30 function of applied strain for SCS craters with aspect ratios of $b/a = 0.25, 0.5$ and 1 . Curves and diamonds

1 represent finite element results at full unloading and pull-off point, respectively. Solid (DMA) and open
2 (MTS) circular dots are experimental data. (d) A contour plot for the normalized suction force at full
3 unloading $\tilde{F} = -\Delta p A_2 / (p_a A_0)$ as a function of b/a and ϵ . The white star highlights the highest suction
4 force in the non-vaporization regime while the capital “V” represents the vaporization zone when $\epsilon > \epsilon_v^0$
5 $= 0.35$.

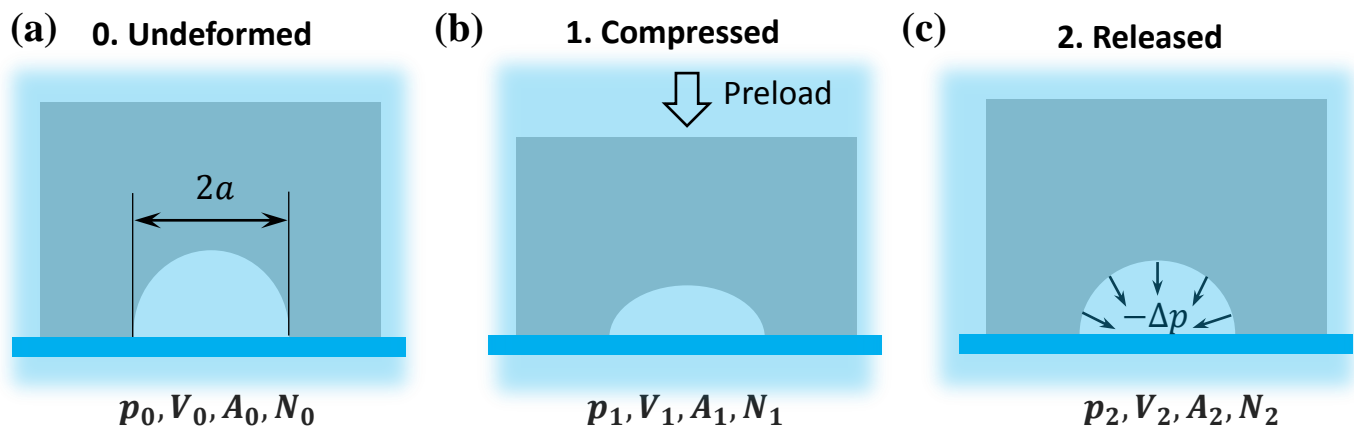
Fig. 1

Fig. 2

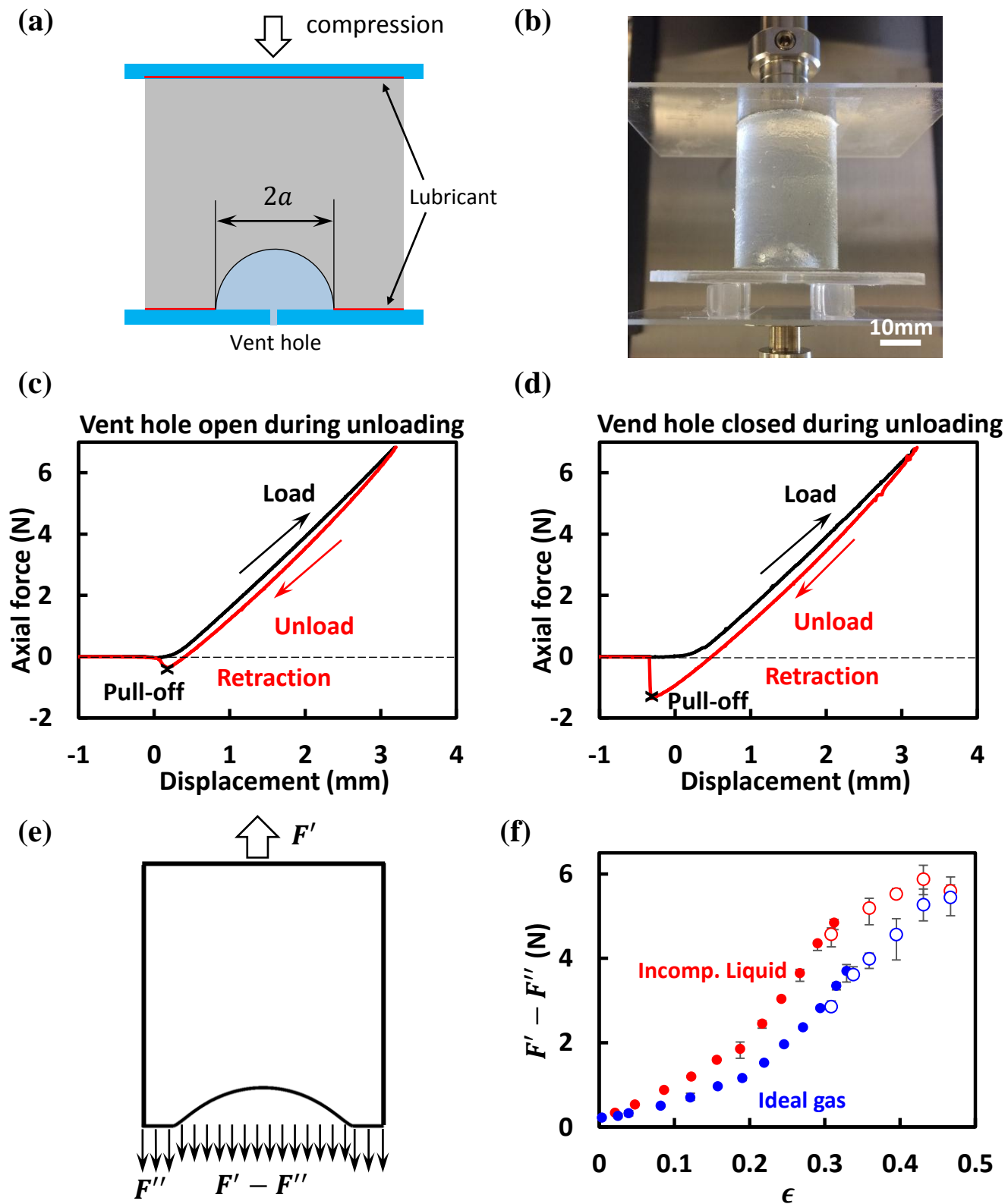


Fig. 3

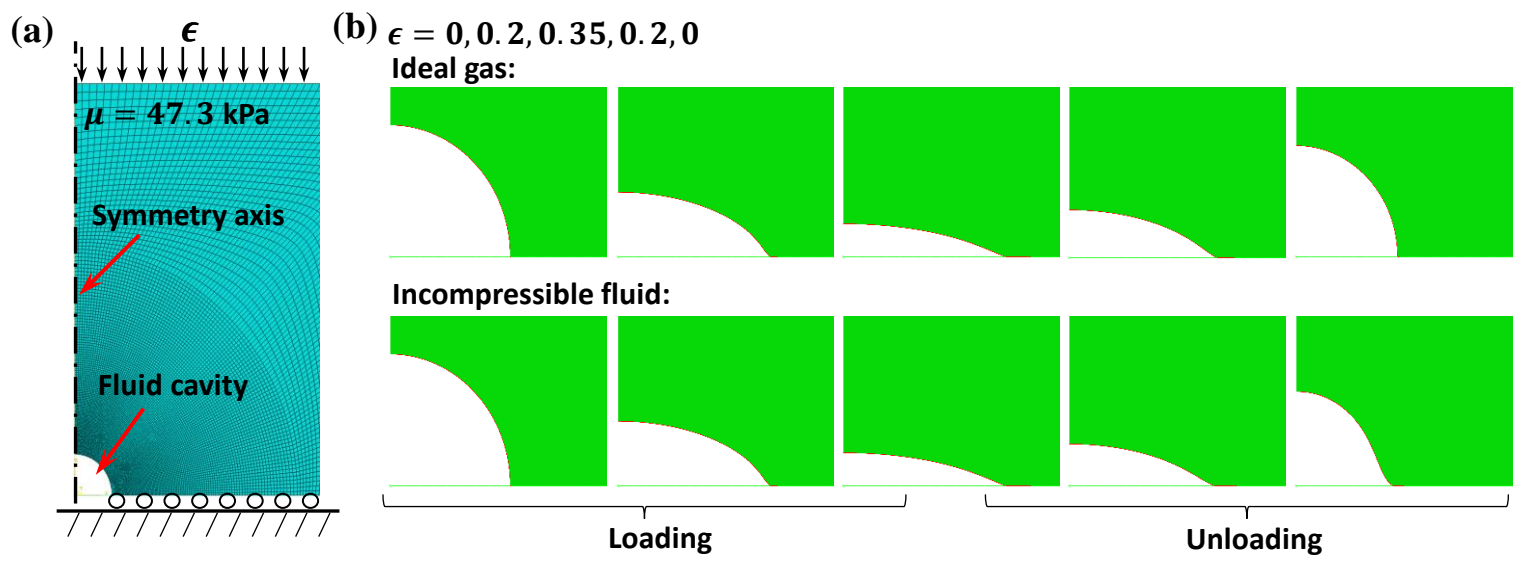


Fig. 4

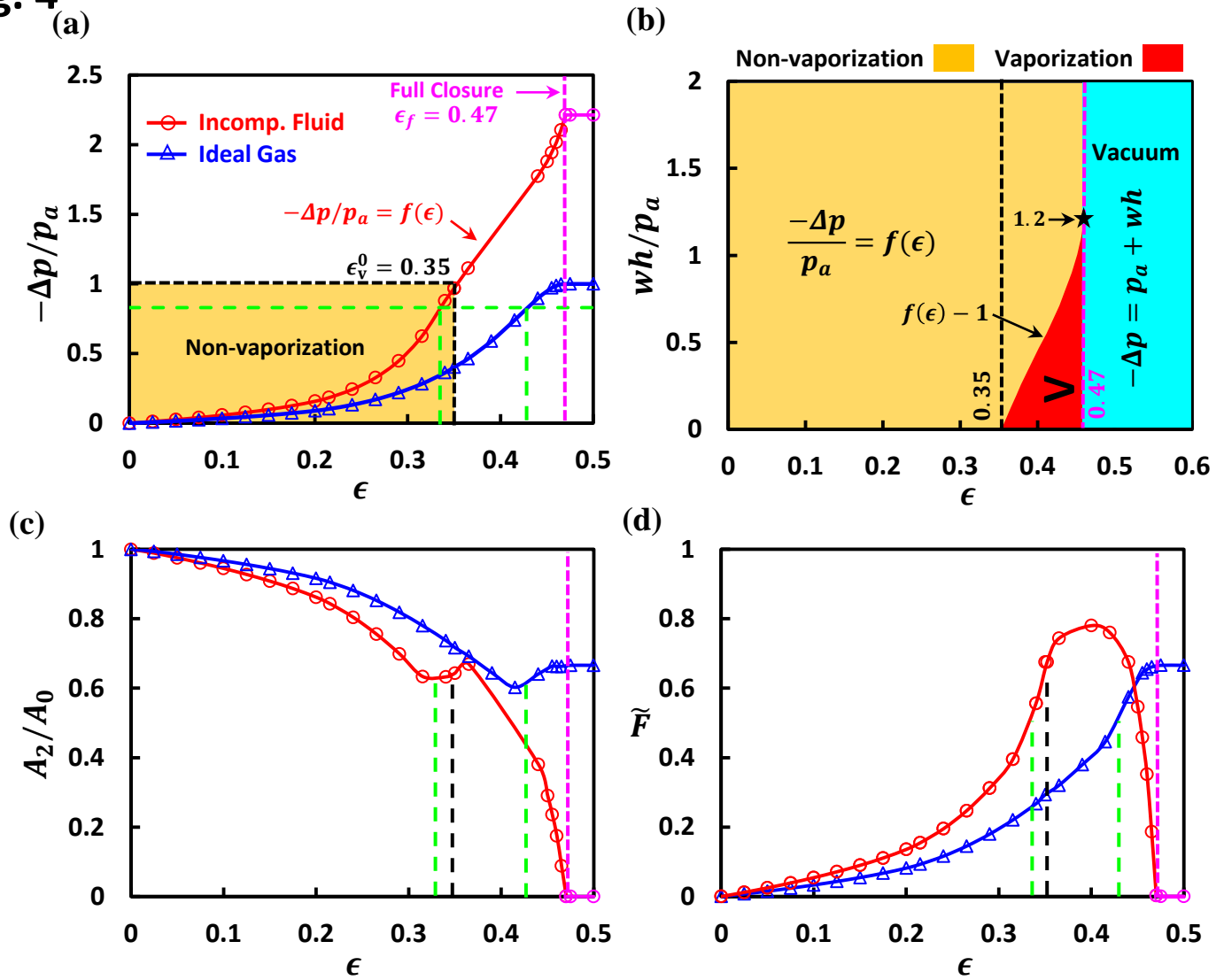


Fig. 5

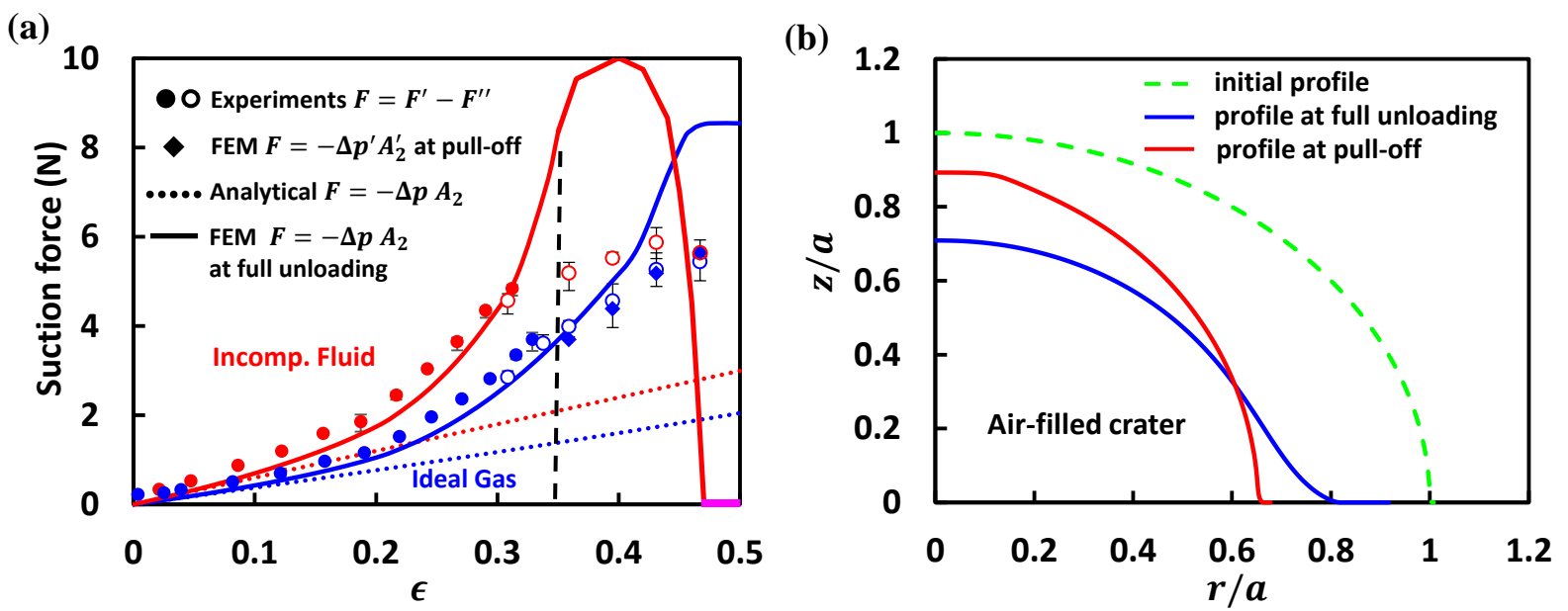


Fig. 6

